Optimized geometry design of a radial impulse turbine for OWC wave energy converters

Mina Saad, Manuel García Díaz, Bruno Pereiras, and José González

Abstract

Opposite to other types of turbine for OWC wave energy converters, like the axial impulse or the Wells turbine, there is scarce information about radial impulse turbines. The interest in radial impulse turbine for wave energy is low because the available research on it shows lower efficiencies than the competitors. On the other hand, radial turbines present several advantageous features that make it a worthy option if the efficiency is improved. The purpose of the present work is to propose a new geometry, not focused on improving the rotor efficiency, but on reducing losses downstream of the rotor. This new design, taking previous geometries as a reference, was based on the classical 2-D angle computations, optimizing the flow and blade angles for both inflow and outflow modes. After setting a balanced agreement between both modes, a numerical model with the new design was mounted on ANSYS Workbench which has allowed to speed up the whole process by using the specific tools set for turbomachines. Taking advantage of the simulation speed provided by the use of this model. A solidity optimization process was performed out on the new geometry to decide the required number of blades and vanes of the proposed turbine. Once, the turbine was well-defined, it has been compared concerning the previous turbine under both, steady and non-steady flow. The improvement has been remarkable, reaching a 10 % in steady efficiency and 6.7 % in non-steady efficiency with respect to the previous geometries.

1

2 Nomenclature

3	A_R	Characteristic area
4	b	Blade span
5	C	Chord length
6	C_A [equation 2]	Input coefficient
7	C_T [equation 1]	Torque coefficient
8	IGV	Inner guide vanes
9	$i = \beta_X - \beta^*_X$	Incidence angle for outflow (X=C) and inflow (X=D)
10	OGV	Outer guide vanes
11	Q	Flow rate
12	r	Radius
13	r_R	Mean radius
14	$S = 2\pi r_{Rotor}/z$	Pitch
15	RMX	Ellipse radius
16	T	Period
17	T_0	Torque
18	$u_R = \omega r_R$	Circumferential velocity at r_R
19	$v_R = \dfrac{Q}{2\pi r_R b}$	Mean radial velocity
20	z	Number of blades
21	***Greek letters***	
22	α	Absolute flow angle

2

| 1	α^*	Guide vanes blade angle
2	β	Relative flow angle
3	β^*	Rotor metal angle
4	$\varepsilon = \beta^*{}_C - \beta^*{}_D$	Deflection angle
5	η [equation 3]	Efficiency
6	η_{Rotor} [equation 4]	Rotor efficiency
7	η_{NS} [equation 7]	Non-steady efficiency
8	$\sigma = C/S$	Solidity
9	ρ	Air density
10	ϕ [equation 5]	Flow coefficient
11	Φ [equation 6]	Flow coefficient amplitude
12	ΔP	Total-to-static pressure drop
13	ω	Rotational speed
14	**Subscripts**	
15	Rotor	Turbine rotor
16	C	Reference surface "C"
17	D	Reference surface "D"
18	**Acronyms**	
19	*BEP*	Best efficiency point
20	*RAM*	Radom access memory of PC
21	*CFD*	Computational fluid dynamics
22	*M#*	Radial turbine series

1

1. Introduction.

Renewable energy has been an important research field in the last few years and is going to be in the next ones, due to the climatic change problem, to reduce carbon dioxide emissions. Within renewables, the exploitation of the ocean wave energy to generate electricity will play an important role as been stated by the international renewable energy agency [1]. Oscillating Water Column (OWC) chambers are well-tested devices to convert wave energy into pneumatic energy which was declared by [2] and [3]. Physically, the OWC system is a fixed or floating structure partially submerged in the sea to trap air above the water level and its exhaust is connected to the atmosphere. Incoming waves impact against the OWC wall, allowing the inner water-free surface to rise and fall. This sea-level oscillation produces a bi-directional airflow that drives a Power Take-Off (PTO), usually a turbine. This is subsequently connected to a generator to produce electric power.

The key criterion for the PTO used in the OWC framework is the ability to absorb energy in both directions of movement. There are two major approaches to achieve that requirement, using unidirectional turbines or self-rectifying turbines. Unidirectional turbines can be installed in couples, which is called Twin Turbines Configuration (TTC) [4], [5], or with an external device that rectifies the flow into a unidirectional one, as non-return valves [6] or the vented OWC [7]. On one hand, TTC has several problems compared to bidirectional turbines as the duplicity of equipment or a more complex geometry of the chamber. On the other hand, the saline environment in which is placed the system reduces drastically the lifetime of the external devices with moving parts. Because of this, the self-rectifying or bidirectional turbine is the most spread PTO for OWC systems [8]. This type of turbine inherently provides a unidirectional rotation for a bidirectional flow as mentioned in [9] and [10]. Bidirectional turbines are divided into two main types: The Wells turbine and the impulse turbine. Wells turbine was introduced by A. Wells in 1976 [11]. With a small flow rate, the Wells turbine power output is low, or even negative, whilst at large flow rates, due to the stall of the blades, the efficiency drops sharply above a critical point as mentioned by [12]. This implies that the Wells turbine can work within only a limited range of flow coefficients as mentioned by [9].

1   The impulse turbine is a self-rectifying turbine with a row of guide vanes on either side of the
2   rotor acting as nozzle and diffuser described by [13], [14], and [15], vice versa under bi-
3   directional flows. In Figure 1, a scheme of an impulse turbine is shown. Despite having a lower
4   peak efficiency than the Wells turbine, it has a wider operative range in which the efficiency is
5   close to the maximum one [16]. Rotor blades and guide vanes design have a direct impact on
6   impulse turbine efficiency. Achieving as much efficiency as possible in the PTO is a field in
7   which researchers are focusing a lot of effort. In the work made by Setoguchi [17] the geometry
8   of two rotor blade profiles and two guide vanes, rows are studied, trying to maximize the turbine
9   efficiency. In the field of radial impulse turbines, geometries, as published in [17], are improved
10   in later works like [18] and [19], in which a higher efficiency was achieved by modifying the
11   geometry and manipulating the tip clearance throughout the turbine. The huge aspect of this
12   analysis seeks to enhance efficiency by reducing the incidence losses associated with the guide
13   vanes row in the downstream of the rotor [18],[20], which substantially penalize overall
14   performance.
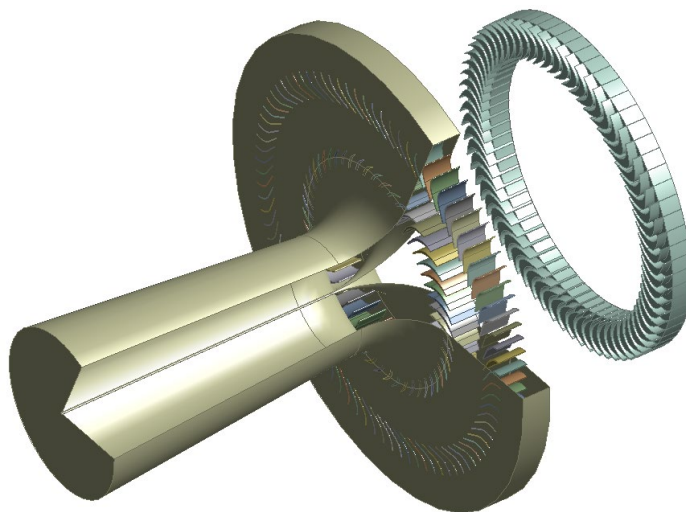
16   **Figure 1 Radial impulse turbine 3-D isometric capture (Present study)**
17   This work aims to achieve an improvement in efficiency by design and test a new geometry of a
18   radial impulse turbine impulse based on the previously published in [18]. This new geometry
19   considers more the exit of the rotor to reduce the losses of the machine, than the rotor efficiency
20   itself. Analysis orientation was maintained to reduce the disparity in pressure around the system
21   to improve efficiency. The new geometry is analysed numerically using a commercial CFD code.
22   Validation was carried out in a previous study using a similar model in [18]. A comparison

5

1   between the base design and the new one is presented in terms of the classical dimensionless

2   coefficients. Also, a study of the flow patterns and losses of the new turbine was developed to

3   illustrate the enhancement due to the design changes and envisaging further optimizations for

4   future works.

2. Materials and Methods

2.1 Dimensionless coefficients and nomenclature

7   In this section, dimensionless coefficients for data processing will be presented by the

8   performance calculation in both steady and non-steady flow conditions steadily addressing the

9   overall efficiency by the torque and input coefficients concerning the flow condition the machine

10   subjected to. All variables included in the equations had been identified in the nomenclature

11   section.

2.1.1 Steady performance

13   Performance evaluations are expressed in terms of the classical dimensionless coefficients:

14   torque coefficient C_T, input coefficient C_A, efficiency η, and rotor efficiency η_{Rotor} in which are

15   all presented against the flow coefficient ϕ. These expressions are specified as:

$$C_T = \frac{T_o}{\rho(v_R{}^2 + u_R{}^2)A_R r_R/2} \tag{1}$$

$$C_A = \frac{\Delta P\, Q}{\rho(v_R{}^2 + u_R{}^2)A_R v_R/2} = \frac{\Delta P}{\rho(v_R{}^2 + u_R{}^2)/2} \tag{2}$$

$$\eta = \frac{C_T}{C_A\, \phi} \tag{3}$$

$$\eta_{Rotor} = \frac{T_0\, \omega}{\Delta P_{(C\text{-}D)}\, Q} \tag{4}$$

$$\phi = \frac{v_R}{u_R} \tag{5}$$

2.1.2 Non-steady performance

22   To be able to evaluate the turbine performance into sinusoidal flow conditions, a classical

23   methodology has been used. Examples of this well-known methodology can be found in several

24   publications as [21] and [6]. Periodic flow conditions will be simulated at constant rotational

25   speed by presuming quasi-steady flow conditions. Equation 9 shows how non-steady efficiency

26   η_{NS} has been calculated (period $T = 15$ s).

$$\phi = \Phi \sin(2\pi t/T) \tag{6}$$

$$\eta_{NS} = \frac{\frac{1}{T}\int_0^T T_o\, \omega\, dt}{\frac{1}{T}\int_0^T \Delta P\, q\, dt} \tag{7}$$

2.2 Geometry generation

Dealing with designing a bidirectional impulse turbine with fixed guide vanes for OWC systems, both axial and radial, is certainly discouraging because the bidirectionality of the flow hinders the use of any traditional technique employed for unidirectional turbines. The unavoidable incidence losses in at least one of the elements, even in the Best Efficiency Point (BEP), penalize the efficiency drastically. On the other hand, works available in the bibliography supplied an important amount of information about the flow pattern inside these turbines, both radial and axial types ([13], [14], [15], [18] and [22]). Intertwining this knowledge with some ideas coming from the traditional design of unidirectional turbines, a model with a balanced performance in both flow directions can be achieved.

The first bidirectional radial turbine for OWC systems appeared, up to the authors knowledge, in 1992 [23]. It was recovered by the group led by prof. Setoguchi in 2002 [24] and later, it was analysed using CFD techniques in [18] and [19]. From the latter, it was known that the flow pattern shows remarkable features to be considered for new designs:

1. The main source of loss, in both inflow and outflow conditions, is large flow incidence at the leading edge of the downstream guide vanes [18], where a strong flow detachment appears, almost choking the flow path [19]. Actually, it is shown in [25] that the optimum position of the GV can lift the efficiency notably.
2. The rotor, in designs from [24] and [18], shows a variable rotor efficiency, depending on the flow coefficient, but being able to reach maximums above 63% in both inflow and outflow performance. Nevertheless, it is stated in [18] that a balanced operation between

inflow and outflow conditions is completely desirable. The rotor loss in the models from [24] and [18] is mainly related to two causes: the first one, especially at low flow coefficients, is the flow incidence at the blade leading edge. Whereas, at large flow coefficients, the tip flow, which in combination with the strong curvature of the blades, induces an early flow detachment in the suction side of the blade [19]. The latter leads to having one-third of the blade span not performing properly, especially during outflow condition when there is an adverse pressure gradient as well.

3. The loss at the elbow during inflow performance is a problem directly related to the inner guide vanes. Nevertheless, it appears to be partially solved by enlarging their length [18], which produces an enhancement in the guidance towards the duct. Nevertheless, the loss associated with the duct, in inflow performance, is above 10% of the total loss even in the BEP.

4. Although it is not included in previous analysis [18], the kinetic energy at the outlet, in both inflow and outflow performance, is a real drawback as it will be shown in this work. It can reach values over 10% of the total loss of the whole turbine.

Hence, looking for minimizing the problems shown in previous designs a new geometry was planned. The strategy applied in this optimized prototype can be summarized in the following lines:

a) Since the incidence loss (proportional to the kinetic energy) in both the guide vanes downstream the rotor and the rotor itself appears to be the most important problem to be solved, it was decided to reduce the rotor blades deflection $(\beta^*_C - \beta^*_D)$, in order to decrease the tangential component of the velocity, thus decreasing the absolute velocity as well. This also allows to increase the setting angle of both rows of guide vanes. On the other, according to Euler equation, this will involve a reduction in the torque generated. Another option to reduce the kinetic energy at the inlet of the guide vanes has been recently presented [26], it consists of placing the guide vanes further. This solution has not been applied in this work to not increase the size of the turbine.

b) The kinetic energy at the outlet, especially during inflow performance, has revealed itself as a real problem, also seen in [7]. Hence, the elbow has been shaped like a diffuser

8

similar to any other inflow turbine. In outflow performance, the loss associated with kinetic energy at the outlet is less important. Besides, the parallel walls at the outer part of the turbine guarantee that the section is directly proportional to the radius. Apart from that, modifying the setting angles of the guide vane to larger values, produces less deflection in guide vanes as well, which is expected to reduce the tangential component of the velocity at the IGV outlet during inflow conditions. Then, the swirl present in the duct at off-design conditions will be less powerful.

c) Suppressing the tip gap in other words has turned to be necessary. Solving this issue is not a problem actually, but it will lead to a different concept in the mechanical design, turning to the shrouded rotor which was successfully tested for a similar structure in [22].

d) The last condition to build the new geometry was that in this case, opposite to what the authors made in the past, the focus is not only on the rotor efficiency. Previous experiences show that any percentual point gained in the rotor efficiency drove towards increasing the loss at the guide vanes at the same rate. Hence, the model presented in this work is focused on achieving a balanced loss distribution between the rotor and the guide vanes.
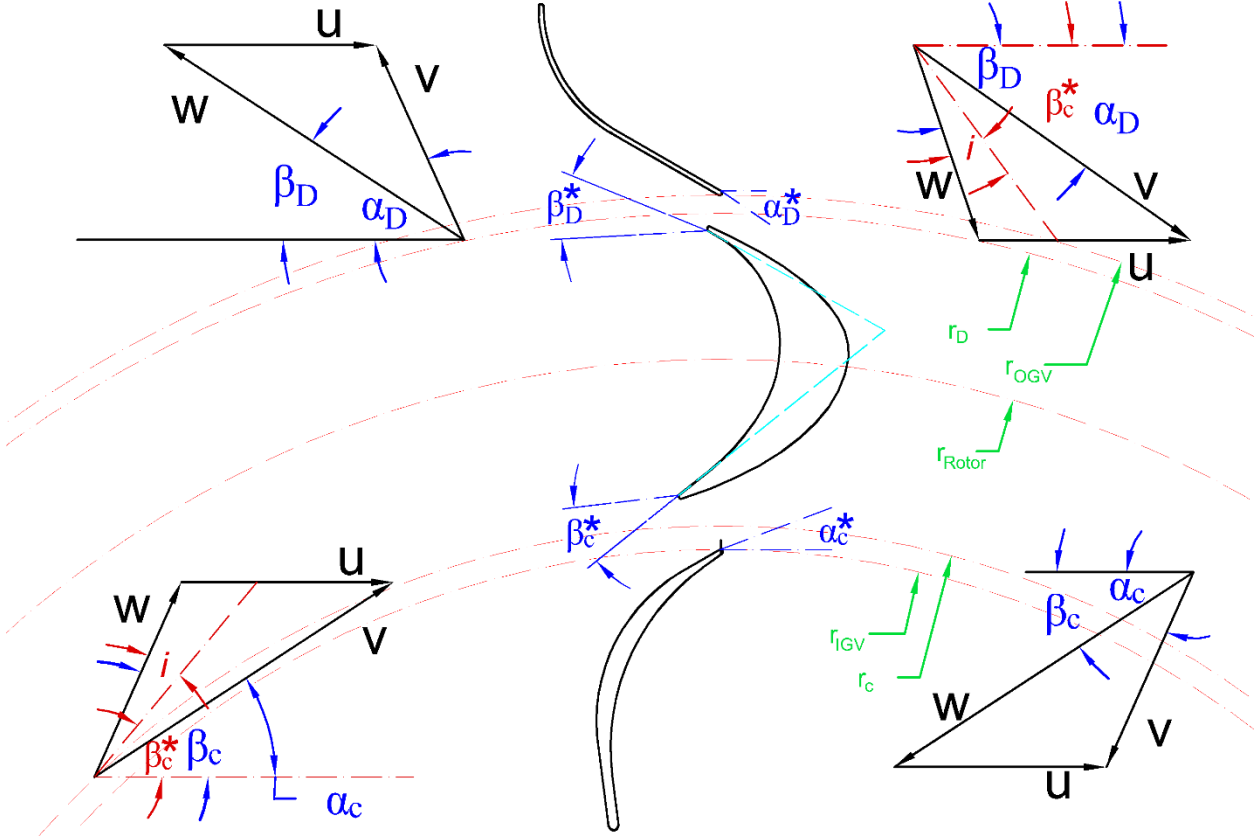
Figure 2 Flow and geometry angles.

The creation of the geometry is based on classical two-dimensional calculations, followed by an analysis to find the optimum solidity.

The slip has not been taken into account since there is a lot of research made on the slip [27] where it is established that the slip factor strongly depends on the number of blades/vanes, which is large enough in this turbine to guarantee a value of the slip factor close to one. This was found in not published data from [18] and [28], where the slip was less than 3%.

1   As the design point to initialize the design process, it has been taken $\phi = 0.75$ as Best

2   efficiency Point (BEP) and the rotation speed was set to 234 rpm. To discard the Reynolds effect

3   in the comparison with previous Radial Impulse Turbines, the mean radius was set to $r_R = 212.4$

4   mm whereas the position of the Guide Vanes, for inner and outer rows, were set to $r_{IGV} = 180.4$

5   mm and $r_{OGV} = 245.4$ mm, respectively. The blade span is 44 mm.

6   In order to obtain a smaller deflection than those present in previous Radial Impulse Turbines

7   [24] and [18], the setting angle of the guide vanes, both inner and outer, was set to 30 degrees.

8   This drives to the utilization of a rotor with less deflection.

9   It is necessary, as it is stated in Figure 2, that both flow directions must be considered since the

10   turbine is equipped with fixed guide Vanes. Nevertheless, the turbine was considered

11   unidirectional, for a design point of $\phi = 0.75$ with zero flow incidence in each performance

12   mode, inflow, and outflow. Hence, according to the two-dimensional calculations, for outflow

13   conditions, the β^*_C should be 52 degrees to receive the flow from the IGV perfectly matched,

14   whereas the β^*_D would be set to 16 degrees to obtain a zero incidence at OGV leading edge.

15   However, considering inflow conditions, following the flow path, β^*_D and β^*_C should be 91 and

16   20 degrees, respectively. Then, β^*_C should be within the range of 20-52 degrees whereas β^*_D

17   within 16-91 degrees. The latter having a broader range due to the lower radial flow velocities

18   and the larger blade speeds.

19   It is known that, for outflow turbines, the incidence loss is relatively insensitive if the incidence

20   angle is between +20° and -20° [29], in line with results for axial turbines [27]. Then, fixing β^*_C

21   to 36°, it is expected those flow coefficients $\phi > 0.65$ show an incidence angle below 20°, so

22   the rotor efficiency during outflow would not be compromised. On the other hand, the incidence

23   during inflow condition at IGV, downstream the rotor, would remain below 25° degrees for

24   $\phi < -1$. Following the same strategy for fixing β^*_D is difficult since the range of β^*_D is much

25   broader. Knowing from previous designs [18] that the OGV is the source of a large amount of

26   loss in outflow performance due to the large incidence, it was decided to sacrifice the incidence

27   at the rotor leading edge during inflow performance. During inflow conditions, incidences below

28   20° at the rotor leading edge are only guaranteed for flow coefficients $\phi < -1.5$, which results

29   in a $\beta^*_D = 30°$. The incidence loss during inflow condition would sever the rotor efficiency, but

for inflow turbines, it is reported that, depending on the geometries, the efficiency would be reasonably insensitive to incidences within the range [+40, -40], see [30]. On the contrary, this β^*_D would lead to remarkable improvement during outflow condition at the leading edge of the OGV, downstream the rotor, where the incidence is maintained below 70° in most of the positive flow coefficient range. Optimized geometry aspects with respect to the previous geometry [18] are mentioned in Table 1 and Figure 3.

Table 1 Geometrical characteristics for each section.

	Previous geometry [18]				Optimized prototype			
	Vane/Blade number	Chord length (mm)	Solidity	Inner/Outer Setting angle	Vane/Blade number	Chord length (mm)	Solidity	Inner/Outer Setting angle
IGV	34	71	2.54	20°	51	60	2.68	30°
ROTOR	51	47	1.78	20° /25°	68	55	2.69	36° /30°
OGV	85	45	2.42	20°	85	54	2.89	30°

12
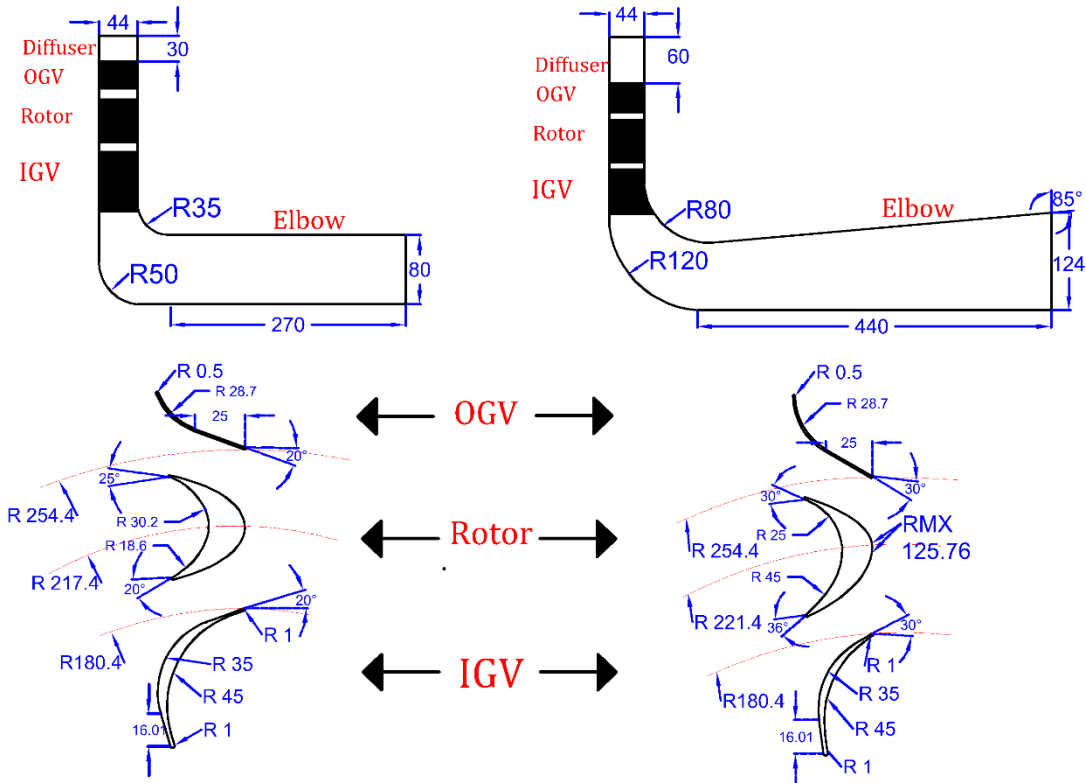
Figure 3 Previous geometry [18] **and optimized prototype dimensional plot.**

2.3 Numerical model

The numerical model presented in this work is an advanced evolution of the CFD work previously published in [24] and [18]. In this paper, it is shown how the model has evolved into a powerful tool, allowing the creation of geometries and carry out the simulations in a linear process chain utilizing the ANSYS Workbench platform, where all the required software is connected: Blade Editor, TurboGrid and FLUENT.

The geometry, following the description in subsection 2.2, is created in Blade Editor containing the whole turbine, both rows of guide vanes, IGV and OGV, the rotor blades, the diffuser, and the elbow. The mesh is generated using TurboGrid, using the ATM optimized "Single Round Round Symmetric" topology, which allows creating of high-quality structured mesh around vanes and blades, totally composed of hexaedrical cells. The mesh structured is shown in detail

Figure 6, where can be seen the refinement made close to the walls in order to guarantee the correct range of y^+. Besides, as it can be seen, the model takes advantage of the axisymmetric relation of the vanes/blades ratio to utilize a periodic domain corresponding to a 1/17 of the whole turbine, thus saving computational resources. A grid sensitivity study was done to show reliability of the numerical model in three different mesh cases 0.5,1.2 and 2 million hexaedrical cells. The percentage of deviation from the maximum number of cells simulated (2 million cells) is shown in Figure 4, and it is clear that 0.5 million cells achieved the least accurate results compared to 1.2 million cells for a deviation of more than 12 % in the C_A. In the 2 million cells comparison case, which is basically zero, 1.2 million cells indicate around 1.5 percent variation in performance which is almost negligible. The final mesh chosen to be employed to obtain the results shown in the following sections was composed of 1.2 million cells to save computational cost concerning the 2 million cell mesh.
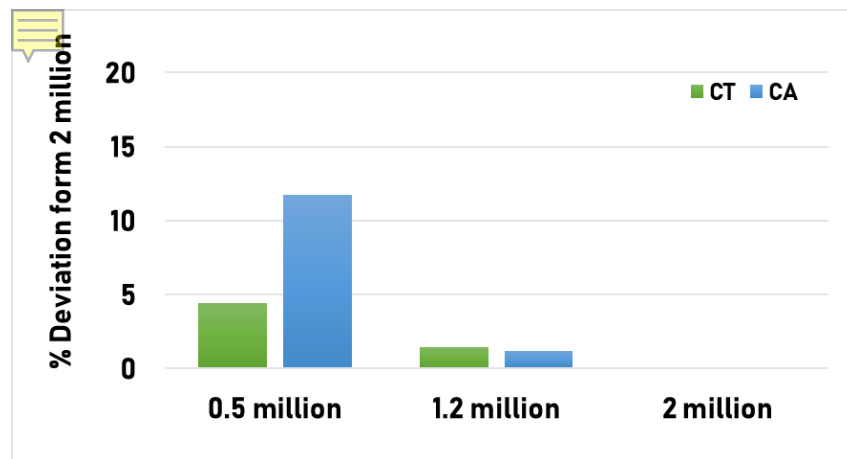
Figure 4 Grid sensitivity study with 2 million cell case as a reference.

The ANSYS Fluent Solver v16 had been used to solve the incompressible fluid conservation equation (RANS). The boundary conditions can be checked in Figure 5, where it is seen the periodic surfaces, and the fixed domains, and the rotating part, which speed was set to 234 rpm. The relative displacement between the rotor and the stators was recreated using the sliding mesh technique, thus two interfaces are separating the rotating domain, which are placed in sections named C and D (Figure 5). Besides, it is shown the boundary conditions used to create the flow through the turbine, sections named A and F are set as velocity inlet and pressure outlet, varying

1   the inlet velocity to obtain different flow coefficients (see Figure 5). Sections A and F permuted

2   their role depending on the desired direction of the flow, outflow, or inflow.

3   The classical k-ε model was chosen for turbulence modelling in combination with enhanced wall

4   treatment. The values of the y^+, once the simulations were done, were that 98.5% of the cells are

5   below y^+ =1, so the reliability of the wall modelling was verified. The time-dependent term is

6   approximated with a second-order implicit scheme. The simple algorithm used for pressure-

7   velocity coupling with the highest order MUSCL scheme for convection terms discretization and

8   diffusion terms.

9   The time-step selected to quantify the relative movement of the grid was 10^{-4} s what results in

10 nearly 50-time steps per blade event. A time step sensitivity analysis was performed with no

11 difference in results between 10^{-3}s, 10^{-4} s, and 10^{-5} s. All the flow rates simulated completed 6

12 rotations of the whole domain, which in combination with setting the residuals in 10^{-5}, resulted in

13 25 hours of computational work per simulation in a machine equipped with an INTEL® I7

14 processor with 3.30 GHz cache along with 16 GB RAM. The variables extracted for

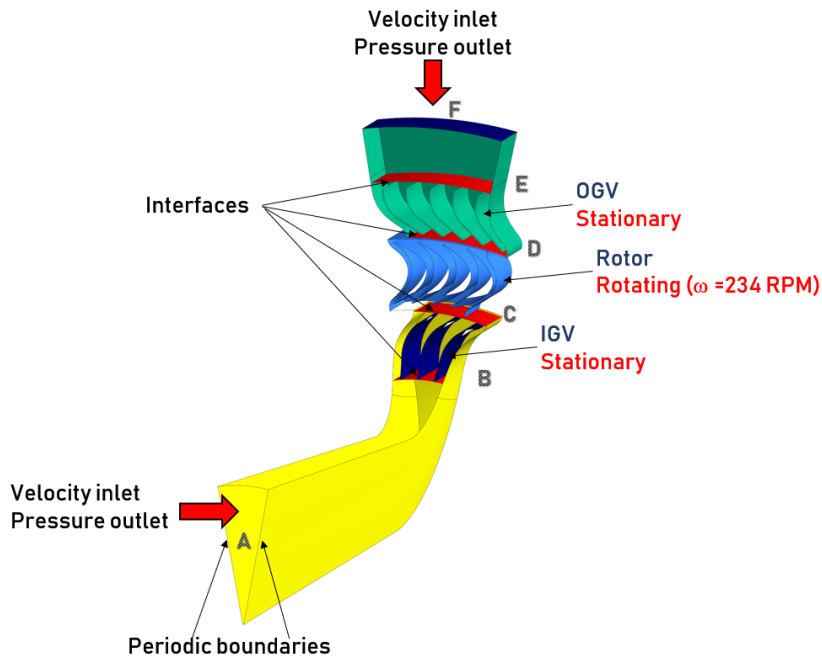15 postprocessing were time-averaged and obtained by using a mass-weighted average.

16

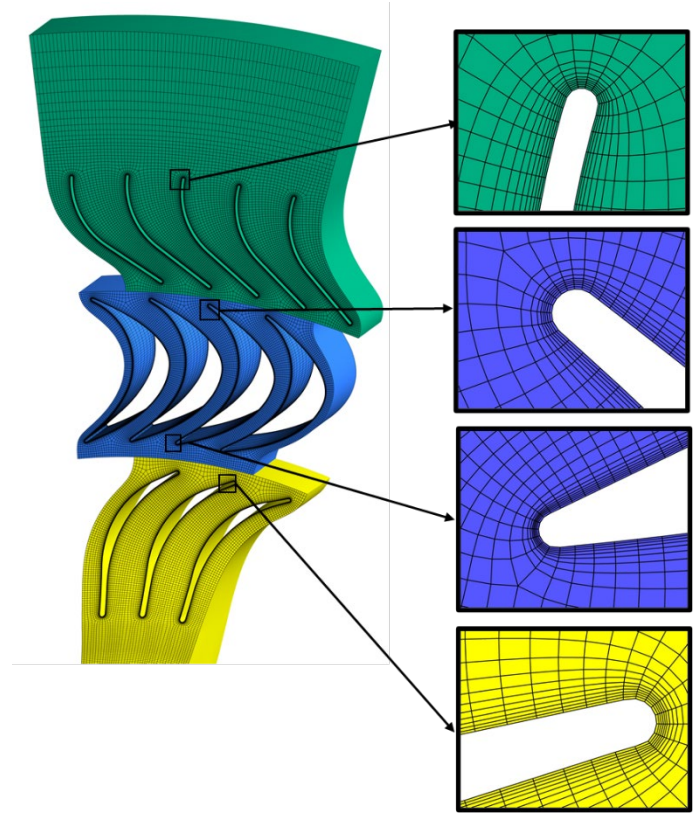**Figure 5 1/17 periodic domain with boundary conditions.**

Figure 6 Detailed model mesh.

1   **2.4 Validation.**

2   Before conducting the main CFD simulations, it is essential to assess the CFD methodology

3   adopted in the present study. To accomplish this, a CFD model is constructed for a radial turbine

4   with available experimental results by [24]. For the reason of comparison, global performance

5   indicators were used. Performance evaluations are expressed in terms of torque coefficient C_T,

6   input coefficient C_A, Consequently, these coefficients have been calculated concerning the flow

7   coefficient ϕ, these expressions which are mentioned earlier in section 2.1.

8   The geometrical data had been illustrated in Table 2 [24], an exact numerical model had been

9   developed using ANSYS workbench to validate our present model, except for a slight decrease

10   in the guide vanes number to cope with the 1/17 periodic domain developed for this study.

11

12

1

2

Table 2 Setoguchi's original geometrical data [24]

	Vane/Blade number		Chord length (mm)	Solidity	Inner/Outer Setting angle
	Experimental [24]	Simulated [Present study]			
IGV	52	51	50	2.29	25º
ROTOR	51	51	54	2.02	19.8º /35.8º
OGV	73	68	50	2.28	25º

Setoguchi's original radial turbine [24]

3

4 Figure 7 and Figure 8 presents the torque and input coefficients respectively, for the present and
5 previous experimental study by Setoguchi [24]. For both inflow and outflow modes, the simulated
6 outcomes are in greater alignment with lower flow coefficients $(0 < \phi < 1)$. During outflow
7 mode, perfect agreement between the numerical model results and the experimental data in both
8 C_T and C_A. However, overestimation to the torque coefficient appeared in the inhalation mode
9 with increasing variance at higher flow coefficients with a maximum value of 25% at $\phi = -1.5$.
10 Torque coefficient aberration had been noted in several publications [31],[7] validating with
11 Setoguchi's original geometry. Although the increase in variance at higher flow coefficients, the
12 CFD findings are relatively consistent with the experimental evidence and provide confidence in
13 the precision of the CFD model used.
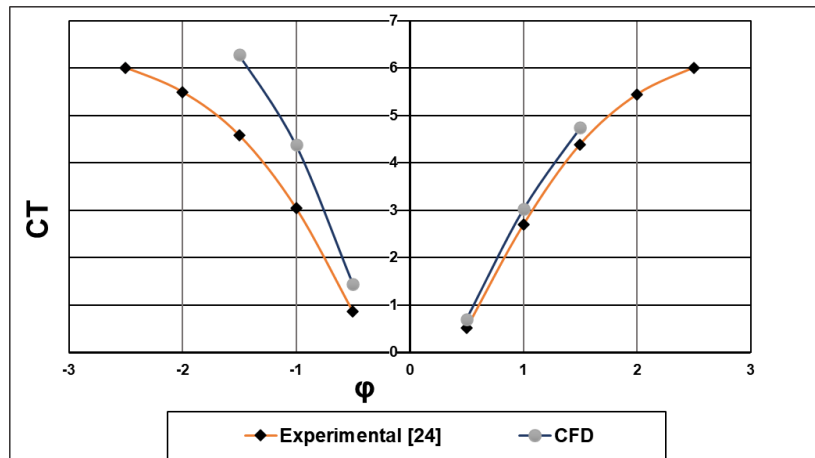
14

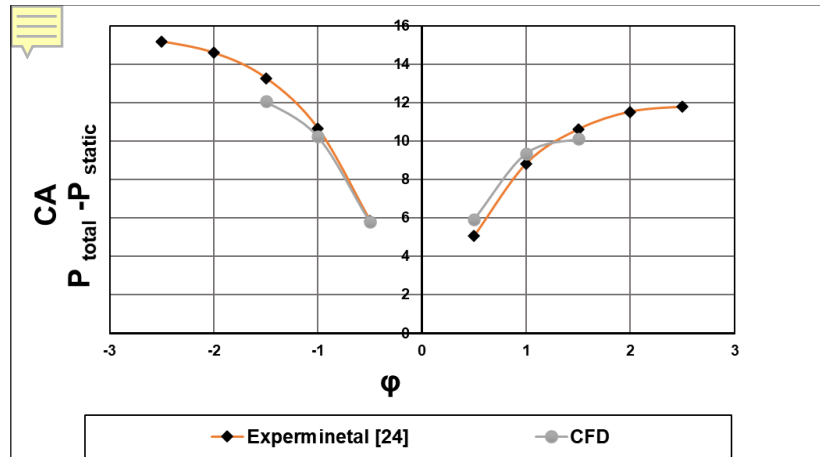15 **Figure 7 Comparing experimental [24] and numerical results for Torque coefficient (C_T)**

17

Figure 8 Comparing experimental [24] and numerical results for input coefficient (C_A).

.

2.5 Solidity analysis.

Accordingly, after settling on the new geometry, solidity analysis was the key to determine the appropriate solidity for the blades and vanes (Inner and Outer) which inconsequence paved the way to better overall efficiency.

In the solidity analysis, different configurations have been simulated to know the influence of the solidity of any part, IGV, OGV, or ROTOR, on the global performance of the machine. Therefore, whereas the solidity of two parts remains constant, the solidity of the 3rd element has been modified. In Table 3 info about the geometries simulated can be found. Note that all the solidities tested correspond to a specific number of blades or vanes multiple of 17 to maintain the periodic domain mentioned in section 2.3.

Table 3 Solidity optimization cases.

Solidity			
	IGV	ROTOR	OGV
Δ IGV	34	68	85
Δ IGV	51	68	85
Δ IGV	68	68	85
Δ ROTOR	51	51	85

18

Δ ROTOR	51	34	85
Δ OGV	51	68	68
Δ OGV	51	68	102

1

2   The different configurations will be named as "xx/yy/zz", being the numbers xx, yy, zz, the

3   elements count in each row, IGV, ROTOR, and OGV, respectively. For example, the first

4   configuration in Table 1 will be 34/68/85. The comparison between different configurations will

5   be made in terms of flow guidance and loss in the element analysed and the element

6   downstream. Moreover, outflow and inflow performance will be studied separately, both for a

7   flow rate coefficient, $\phi = 1$.

8

9   **2.5.1   IGV**

10   Three configurations are analysed to determine the effect of the solidity in the performance of

11   the IGV, those are equipped with 34, 51, and 68 vanes, whereas the rotor and the OGV remain in

12   68 and 85, respectively.

13   Outflow performance will be studied first. In Figure 9.A, it is shown the effect of the solidity

14   change in terms of flow guidance, plotting for $\phi = 1$ the flow and metal angles, α_C and α_C^* ,

15   against the IGV vane count. As it is seen, the angle has a slight dependency on the solidity,

16   reducing the flow angle by 8 degrees if the number of vanes goes from 34 to 68. Therefore, as

17   expected, the flow guidance improves as the solidity increases. Note that, at the largest solidity,

18   the flow angle is more deflected than the guide vane metal angle. This effect, which is present in

19   both the rotor and the OGV as well, is derived from the wake mixing after the trailing edge of the

20   IGV vane as mentioned in [32] appendix 3. This effect appears when the passage section is

21   narrowed due to a large solidity, increasing the importance of the wake. A more detailed

22   explanation of this phenomenon can be found in [32] appendix 3. The relative angle β_C is shown

23   in Figure 9.B, following the same trend as the absolute angle, and it is clear from this figure that

24   the flow guidance towards the rotor is not optimal, as expected. On the other hand, looking at

25   Figure 10, where the total-to-total pressure loss is plotted it is possible to appreciate that the

26   increase of the solidity leads to a slight rise in the IGV loss, which is associated with friction

1   losses. Besides, the rotor loss also plotted in Figure 10, while escorting IGV and rotor losses

2   together, results show a minimum in the configuration equipped with 51 vanes. Although the

3   differences are small, around 1%. Thus, the variation in the incidence angle when changing the

4   solidity does not make much influence on the rotor loss, which agrees with [29], where it is

5   stated that incidences of ±10 degrees do not affect the rotor performance.

6
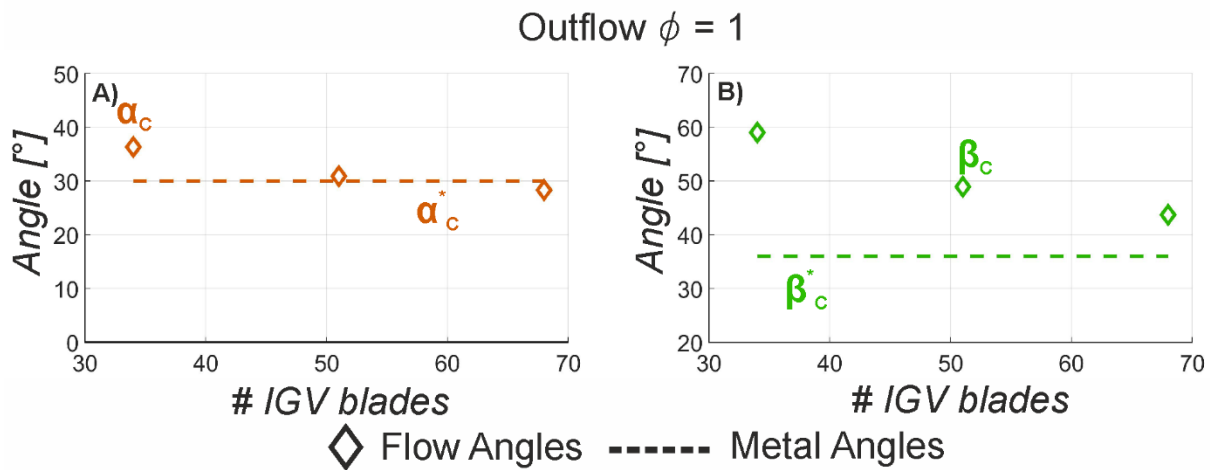
7   **Figure 9 α and β angle at section C, at $\phi = 1$, in different IGVs count.**
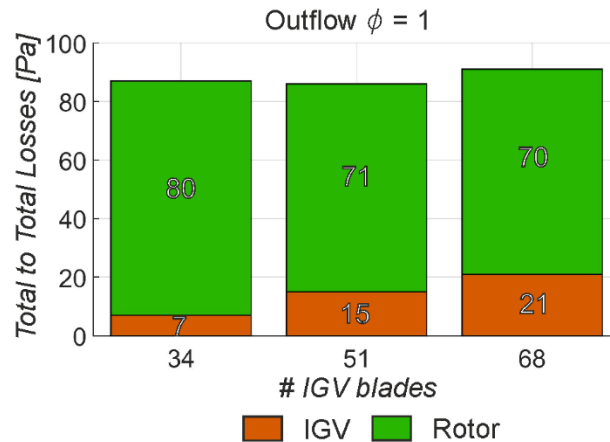
8

9   **Figure 10 Energy loss in IGV and Rotor with respect to IGVs count, at $\phi = 1$**

10

11 During inflow performance, the conclusions are similar to that extracted for outflow

12 performance. Figure 12 shows that the guidance towards the elbow, which the element placed

13 downstream during inflow performance, is almost unaffected by the solidity. The flow angle in

14 section B, α_B , is close to a radial direction even for the 34 vanes configuration.

1   The results related to total-to-total pressure loss for IGV and the elbow during inflow

2   performance are presented in Figure 12. Since, for $\phi = -1$, the flow incidence at the IGV leading

3   edge is close to zero, the rise in the loss within the IGV is related to friction. Whereas the loss in

4   the elbow reveals that the α_B shown in Figure 11 is of some importance. When the flow angle

5   differs from the radial direction, the losses in the elbow increases, which strongly indicates that

6   configurations with a lower count than 34 blades are strongly not recommended with respect to

7   the elbow element (Figure 12). Not purely centripetal flows create a large amount of loss in the

8   elbow, as it was shown in [18].

9   Considering the results in both, inflow, and outflow performance, it is clear that the IGV should

10 have between 34 and 51 vanes. Nevertheless, the differences for both IGV configurations are

11 almost negligible. With the same alignment and losses in the elbow section as the 68 vanes count

12 as illustrated in Figure 11 and Figure 12, leaving the choice between the 34 and 51 vanes

13 comparing both in terms of the overall efficiency in the outflow mode at $\phi = 1$,(Figure 13), it is

14 the 51 IGV will have the preference with the superiority of 2.5% in terms of overall efficiency

15 more than the 34 vanes.

16
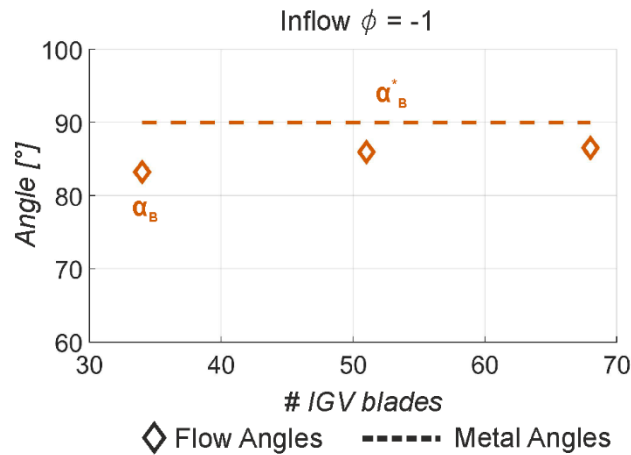
17   **Figure 11 α angle at section B with different IGVs count in $\phi = -1$**
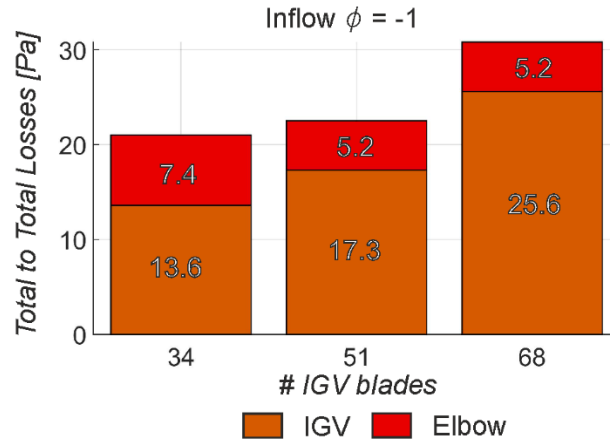
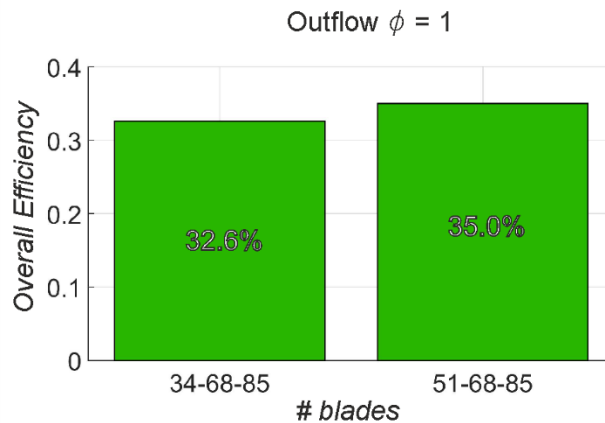Figure 12 Energy loss in IGV and Elbow with respect IGVs count in $\phi = -1$

Figure 13 Overall efficiency in the outflow mode at $\phi = 1$

2.5.2 ROTOR

Three different configurations (Table 3) equipped with 34, 51, and 68 blades, were analysed to determine the influence of the solidity of the rotor. The solidity of both IGV and OGV remains equal.

Apart from being determinant from the point of view of the loss generated, it is critical since correct guidance of the flow also determines the torque on the rotor blades. Therefore, analysing the influence of solidity of the rotor requires both losses and overall efficiency.

1   As before, outflow performance is analysed first. Figure 14 shows the relation between α and β

2   angles in section D (downstream the rotor) with respect to the solidity of the rotor. It is clearly

3   seen in Figure 14.A that the higher the solidity, the better guidance but here, as it happened in the

4   IGV, there is an over-guidance of the flow as well for the largest solidity. The explanation,

5   previously mentioned, is related to the relative position of the wall with respect to the velocity

6   direction ([32] appendix 3). Nevertheless, the difference between 51 and 68 blades is relatively

7   small so the torque produced is similar in these two configurations. It is more revealing how this

8   guidance affects the absolute angle α_D, see Figure 14.B. There is a clear mismatch between the

9   flow angle and the OGV vane angle (downstream in outflow performance) that creates an

10   important amount of incidence loss at the vane leading edge. Looking at Figure 15, concerning

11   the loss in the OGV, it can be concluded that increasing the solidity of the rotor is extremely

12   positive since most of the loss in this element is coming from a large incidence angle. However,

13   adding the loss in the rotor to the picture, the scenario is slightly different. Increasing the solidity

14   of the rotor reduces the flow passage section between blades, increasing the velocity, thus

15   friction loss and wake intensity increase as well. According to the results in Figure 15, using 68

16   blades would be the most favourable configuration for outflow performance. However, due to

17   the slightly larger flow deflection achieved by the 68 blades, this configuration shows a lower

18   energy loss than the 51 bladed rotors for the rotor and the OGV losses added together. Therefore,

19   the most advantageous configuration for outflow performance is the 68 bladed rotors by 5%

20   more than the 51 bladed rotors, concerning Figure 16 plotting the overall turbine efficiency for

21   the three configurations of different rotor count 34, 51, and 68.
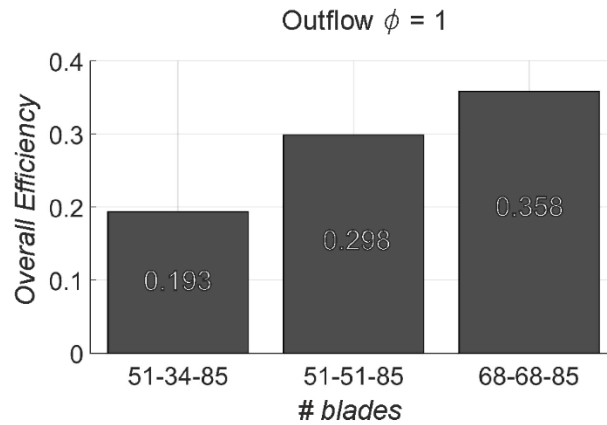

22
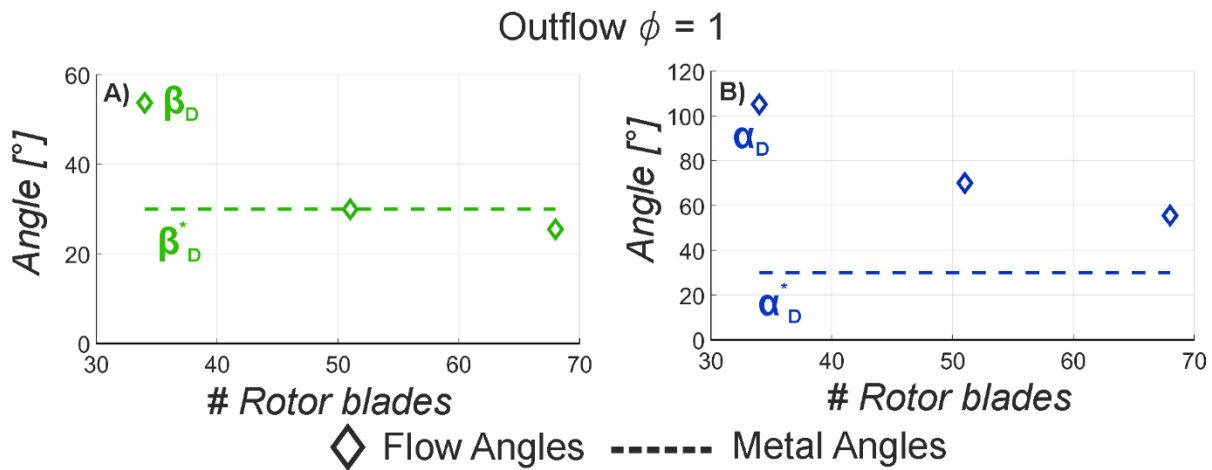
Figure 14 *α* and *β* angle at section D at *ϕ* = 1 in different ROTORs count.

Outflow *ϕ* = 1

2
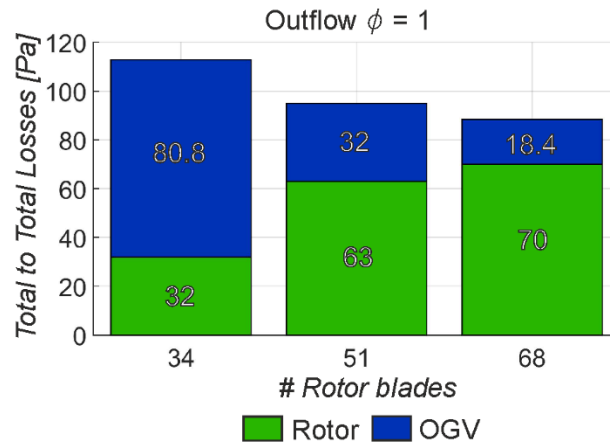
Figure 15 Energy loss in ROTOR and OGV with respect to ROTORs count in *ϕ* = 1.

Outflow *ϕ* = 1

4

5   **Figure 16 Overall efficiency for outflow mode at *ϕ* = 1**

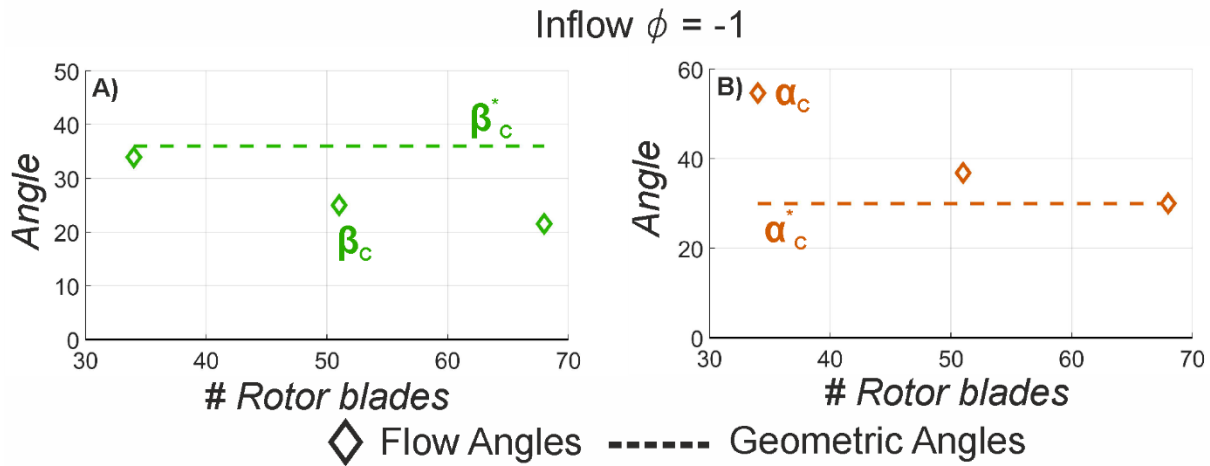6   **for 51-34-85, 51-51-85 and 68-68-85 solidity configurations.**

7   Secondly, the analysis is made during inflow performance. Figure 17.A shows a clear over-

8   guidance of the flow at the rotor trailing edge, even the lowest one of 34 blades manage to guide

9   the flow correctly. This is not a real surprise since, in [19], it was reported that the rotor of this

10   kind of machine managed to make good guidance of the flow at the outlet, especially during

11   inflow conditions due to the favourable pressure gradient along the rotor passage. Nevertheless,

12   it is strengthened in this rotor geometry, which is beneficial to reduce the incidence loss

13   downstream in the IGV. Figure 17.B shows that the mismatch of the incidence angle with respect

14   to the metal angle of the leading edge of the IGV is reaching almost zero for the largest rotor

15   solidity.

On the other hand, looking at Figure 18, where the loss of the rotor and IGV are plotted, it can be seen that the loss of the rotor is being affected more severely than the loss of the IGV by the rotor solidity. Actually, increasing the solidity reduces the passage section between blades, which causes more friction loss and increases the intensity of the wakes. This leads to, in terms of loss, the 34-blade rotor looks more profitable in terms of loss in the rotor element only, otherwise, the effect is been addressed in the IGV element generating more energy losses than the rotor itself. Also, the torque generated is lower than the configurations with larger solidity. Looking at the overall efficiency in Figure 19, 51 bladed rotor improves the other solidities by 2% approximately.
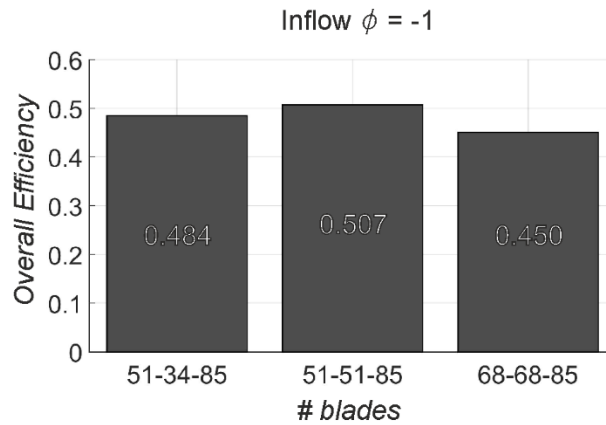

Figure 17 α and β angle at section C, $\phi = -1$ in different solidities.

25
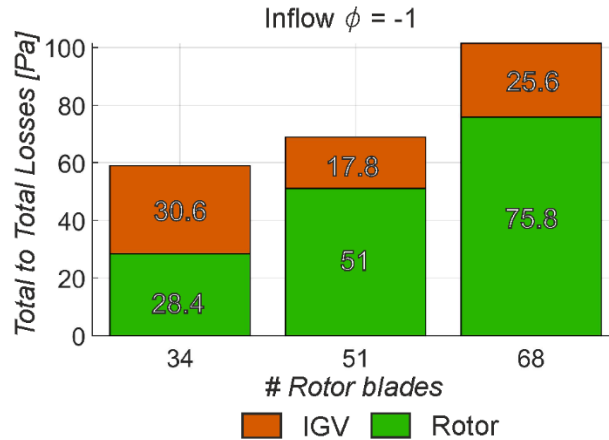
Figure 18 Energy loss in ROTOR and IGV with respect to ROTOR solidity in $\phi = -1$.

Figure 19 Overall efficiency in the inflow mode ϕ = -1 for 51-34-85, 51-51-85, and 68-68-85 solidity configurations

2.5.3 OGV

As reported in Table 3, the analysis of the solidity of the OGV has been made by simulating three configurations with 68, 85, and 102 vanes respectively whereas the solidities of the IGV and the rotor remain equal between configurations.

The results have revealed that the OGV solidity of this turbine has not much impact on outflow performance. Figure 20 shows that the effect of the OGV solidity on the OGV loss, incidence, and friction, and on the diffuser, mainly wake mixing. The differences are really small compared to the total loss of the whole machine, probably caused by the low velocity of the flow in this

1   section. Nevertheless, according to the results, placing 68 vanes in the OGV seems the best

2   option from the point of view of outflow performance.
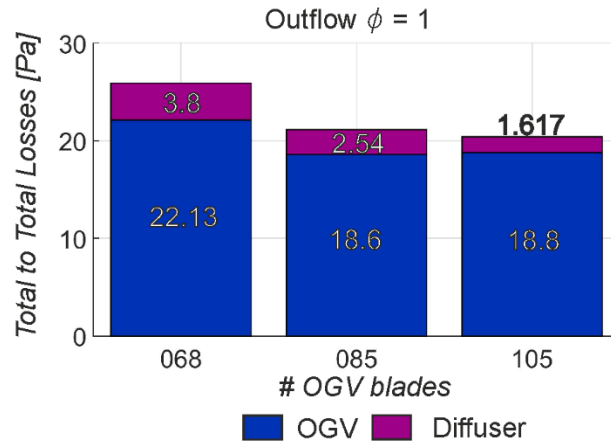
3

4   **Figure 20 Energy loss OGV with respect to OGV solidity in $\phi = 1$.**

5   On the other hand, during inflow, it was expected to see bigger importance due to having the

6   rotor placed downstream of the OGV. However, this expectation was not confirmed since, as it

7   can be seen in Figure 21, the influence of the OGV solidity on the guidance is extremely slight.

8   This is corroborated by the losses in the OGV and rotor elements (Figure 22), which remain

9   constant non-dependent on the OGV solidity. Hence, 85 vanes in OGV were taken as a definitive

10   solidity.

11
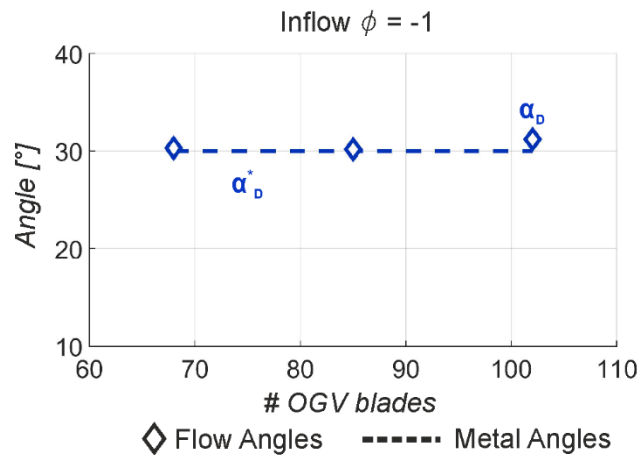
12   **Figure 21 α angle at section D, at $\phi = -1$, in different solidities for OGV.**
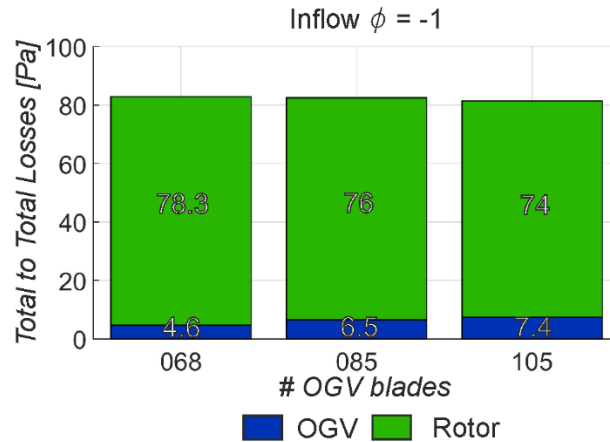
13

Figure 22 Energy loss in OGV and ROTOR with respect to OGV solidity in $\phi = -1$.

Pertain to the solidity analysis conducted in the three elements of the radial turbine (IGV, rotor, and OGV), and with the aid of the flow and metal angles agreements. It has been identified that the most appropriate solidity for each element to go on further studies among steady and unsteady flow conditions are 51,68 and 85 for IGV, rotor, and OGV, respectively.

3. Results

The geometry of the optimized prototype has been defined, the vanes and the blades can be seen in Figure 3, and the solidity of each row was chosen according to the analysis done, being 51, 68, 85 for IGV, rotor, and OGV, respectively. Then, a complete set of simulations were carried out to assess the whole performance curve, which is presented in this section. These results obtained for the optimized prototype are compared to the previous radial impulse turbines, [18] and [24], in terms of dimensionless coefficients from section 2.1.

3.1 Steady performance

The comparison in steady performance has been made comparing the results of the proposed optimized turbine with respect to the best radial turbine published, see [18]. As seen in Figure 23, the optimized prototype shows lower values of C_T for the same flow rate coefficient in both performance modes, inflow, and outflow. This reduction was expected, coming from the lower flow deflection made by the rotor blades. This fact is more significant in outflow mode, where the C_T is reduced by a value of 46% at $\phi = 2$.

On the other hand, it was stated in section 2.2, that the main aim is enhancing the efficiency by reducing losses, not increasing the torque. This is clearly shown in Figure 24, where the input coefficient in the optimized prototype is compared to the previous geometry. It is obvious that the C_A has been greatly reduced, reaching a maximum reduction of 56% for $\phi = -2$. Note that the C_A contains both the loss and the useful energy, so it can be deduced that some part of the reduction comes from decreasing the torque.

In order to obtain a good measure of the improvements done, it is necessary to see Figure 25, where total-to-static efficiency is shown. The considerable increase in efficiency gained during inflow performance with respect to the previous geometry is the most remarkable fact. This improvement in inflow mode, about 9% for the whole range of flow coefficients simulated, is reached because the torque reduction shown in Figure 23 is clearly compensated by a reduction of the pressure difference across the turbine achieved by the new optimized prototype, as it can be deduced from Figure 24. Summing up, the increase of efficiency in inflow is obtained without lessening the efficiency achieved in outflow mode. Even if during outflow the maximum efficiency has not been improved, the range of flow rates showing efficiencies close to the maximum has been extended.

Aiming to understand if the proposal made in subsection 2.1 were correct, rotor efficiency is plotted in Figure 26, comparing the optimized prototype with the previous geometry and it was found that the new geometry has less rotor efficiency in both outflow and inflow modes by a maximum difference of 8 % and 15 % respectively. However, as it was shown in Figure 25, the efficiency of the whole machine has increased, thus the low rotor efficiency was compensated by the loss reduction in the rest of the elements, which was the main aim of the design as was

1   explained in subsection 2.1. After conveying results, evidently, the new geometry represents a

2   great improvement with respect to the previous geometry in terms of steady results.
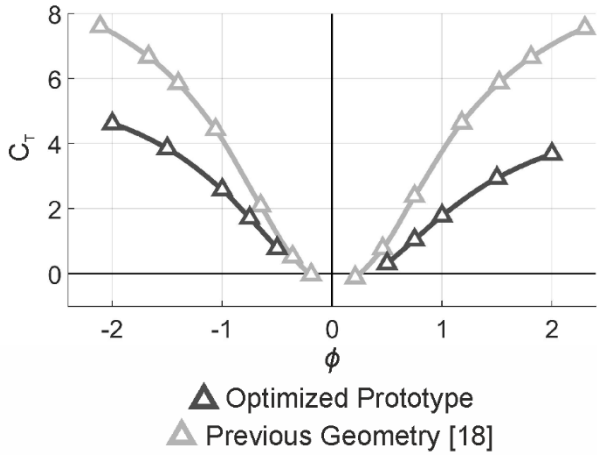
3

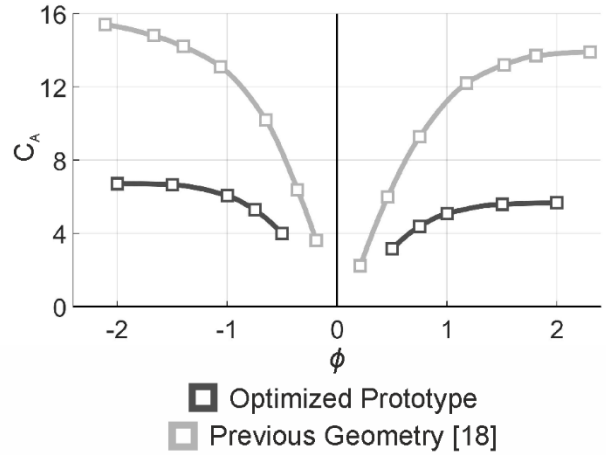**Figure 23 Torque coefficient optimized prototype VS previous geometry** [18]**.**

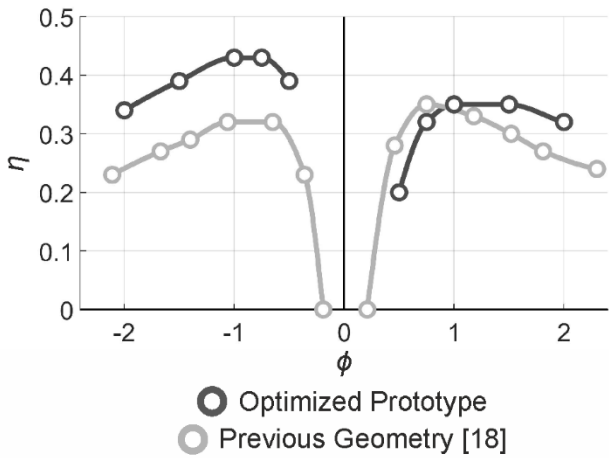**Figure 24 Input coefficient optimized prototype VS previous geometry** [18]**.**

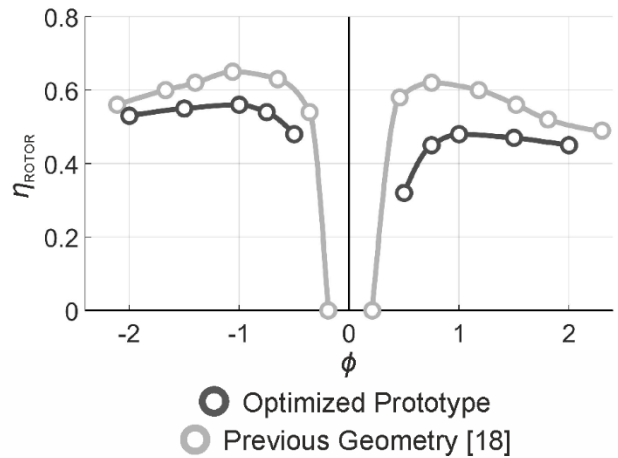**Figure 25 Steady total to static efficiency; optimized prototype VS previous geometry** [18]**.**

Figure 26 Rotor efficiency optimized prototype VS previous geometry [18]**.**

4

5

6

7

8

30

1   **3.2 Non-steady performance**

2   Figure 27 presents the non-steady efficiency, calculated as it is indicated in equation 9 in

3   section 2.1.2, concerning the amplitude of the non-steady flow coefficient stated in equation 8. In

4   this figure, it is possible to see that the optimized prototype had a fair advantage over the

5   previous geometries with an average increase of 6.7 % over the turbine from [18]. According to

6   these results, the new design strategy of the optimized prototype, based on reducing loss at the

7   guide vanes, has proved to be reliable to be considered in future works.
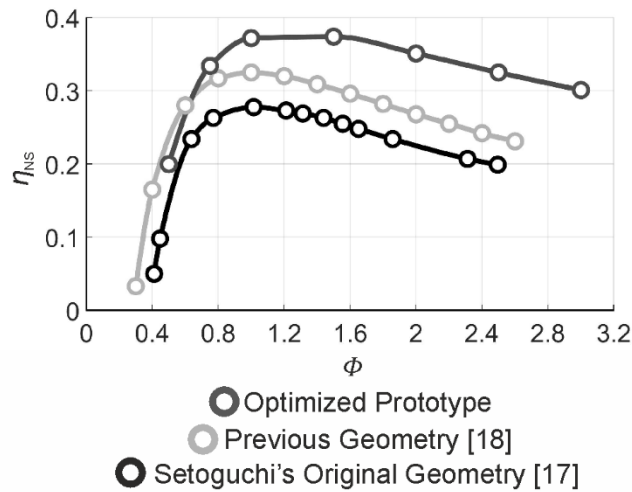
8

9   **Figure 27 Non-steady efficiency for the optimized prototype,**

10   **the previous geometry** [18] **and Setoguchi's original geometry** [24]

11

12   **3.3 Analysis of the flow pattern**

13   In this section, an analysis of the flow pattern is presented, focused mainly on the loss

14   distribution among the different parts of the turbine. These loss distributions are extracted from

15   the steady simulations made. Moreover, an explanation of the main sources of losses is supplied

16   employing the flow angles and total pressure contours.

17

18

19

1   **3.3.1 Outflow**

2   Outflow, according to the nomenclature in Figure 5, starts from section A at the elbow till it

3   reaches section F at the diffuser. The two main sections to analyse the flow pattern are upstream

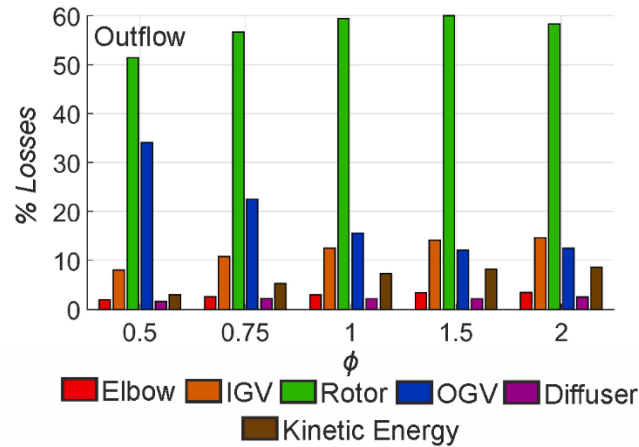4   (section C) and downstream (section D) the rotor as illustrated in Figure 5.

5

6   **Figure 28 % energy loss in outflow per turbine component.**

7   In Figure 28, it can be seen the loss distribution for the outflow mode in terms of percentages. In

8   this figure it is possible to observe that the rotor is the main source of loss of the turbine, always

9   generating 50-60% of the losses for the whole range of flow rates coefficients. This fits with the

10   fact that the turbine has been designed to minimize the losses downstream of the rotor, instead of

11   optimizing the rotor itself, it was evidently noticed earlier for optimized prototype deficient rotor

12   efficiency when compared with previous geometry in Figure 26. OGV showed a rising

13   performance while increasing the flow coefficient, reducing losses in the OGV section by about

14   20% from$\phi = 0.5$ to $\phi = 2$. This is the reason why the steady efficiency of the turbine (Figure

15   25) during outflow performance achieves the maximum for a relatively large flow coefficient.

16   Kinetic energy losses get larger at the turbine outlet when the flow coefficient increases as

17   expected.

18   In order to carry out a comparison between the optimized geometry and the previous one from

19   [18]. the loss distributions for two flow coefficients, one close to the best efficiency point

20   ($\phi = 0.5$), and the other is a large flow coefficient ($\phi = 2$), are presented in Table 4. Differences

21   at the elbow are easily explained considering lower overall losses for the optimized prototype,

22   which results in a larger percentage if the absolute loss is the same. In case of the IGV, it has a

better percentage of energy losses in both lower and greater flow coefficients. This improvement
comes from the less flow deflection made in the vanes, which allows using shorter vanes. The
rotor of the optimized turbine shows the expected larger values of energy losses since it has not
been the priority in reducing losses during the design process. This is clearly marked for large
flow coefficients. Nevertheless, it should be underlined that the greater percentage of losses is
partially caused by the lower overall loss of the whole turbine. OGV performs much better in the
optimized turbine (Table 4), especially for greater flow coefficients, decreasing the total energy
losses. Kinetic energy has been reduced at the outlet, due to it has a lower tangential component
after increasing the length of the trailing edge of the OGV with respect to previous geometry
(Figure 3). But it remains a remarkably secondary source of loss.

Table 4 previous geometry [18] and optimized prototype energy losses percentage in outflow mode per turbine element

|	Previous geometry [18]		Optimized prototype	
	$\phi = 0.5$	$\phi = 2$	$\phi = 0.5$	$\phi = 2$
Elbow	1.71	2.90	1.93	3.43
IGV	12.3	17.77	8.04	14.62
Rotor	46.6	40.12	51.39	58.35
OGV	35.67	25.07	34.11	12.49
Diff	0.34	3.2	1.57	2.53
Kinetic energy	4.01	10.94	2.96	8.58

The contours of total pressure around section C for two flow coefficients ($\phi = 0.5$ and $\phi = 2$)
are shown in Figure 29, where can be seen the interaction between the IGV and rotor blades in
outflow mode. Several phenomena worth to be mention can be seen in the contours, the first one
is the flow detachment produced at the blade leading edge at a low flow coefficient (Figure
29.A). It leads to a strong gradient if total pressure that is related to incidence loss since, as it is
shown in Figure 30.B where the relative angle is plotted, there is a mismatch of 50° between
flow angles and the metal angle $\phi = 0.5$. That drives to boundary layer separation inside the
rotor passage, consequently choking a quarter of the passage. On the other hand, IGV is showing

1   good guidance of the flow (according to Figure 30.A) for the whole range of flow coefficients.

2   While for the higher flow coefficients ($\phi = 2$) presented in Figure 29.B this same effect is less

3   intense as the flow angles tend to match metal angles (Figure 30.B). However, in this case, the

4   intensity of the pressure gradient in the wake draws attention immediately because a strong

5   interaction between the blade and the wake is produced. Placing IGV more separated from the

6   rotor could be an interesting work in the near future, in order to reduce the interaction which

7   surely is a source of loss.
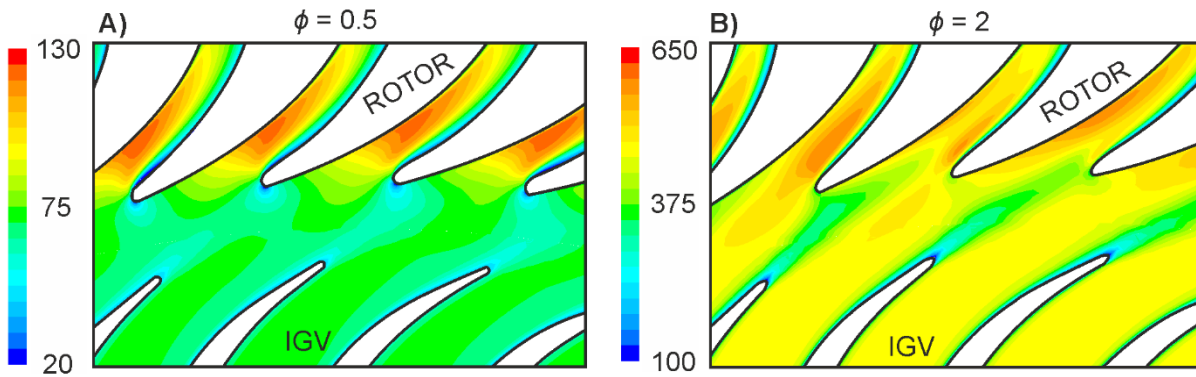
8

9   **Figure 29 Total pressure contours in section C for $\phi = 0.5$ and $\phi = 2$**
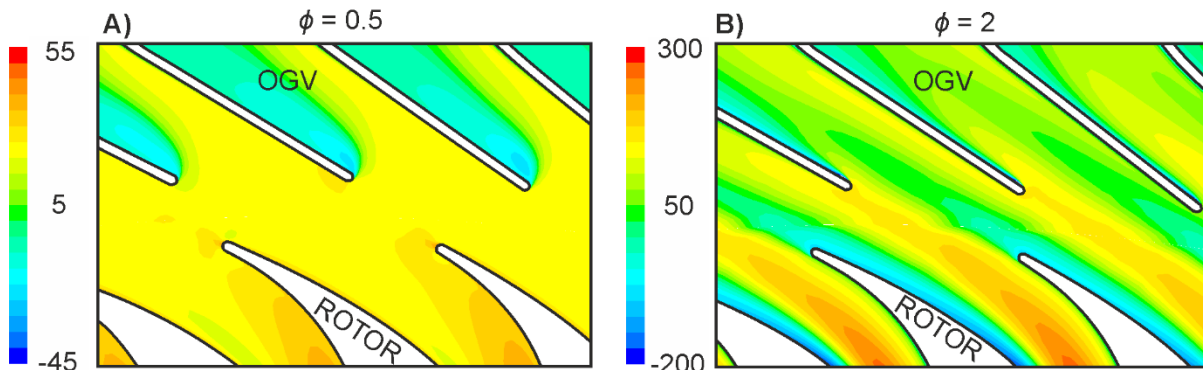
10   **with a colour map scale of 1:5, respectively.**
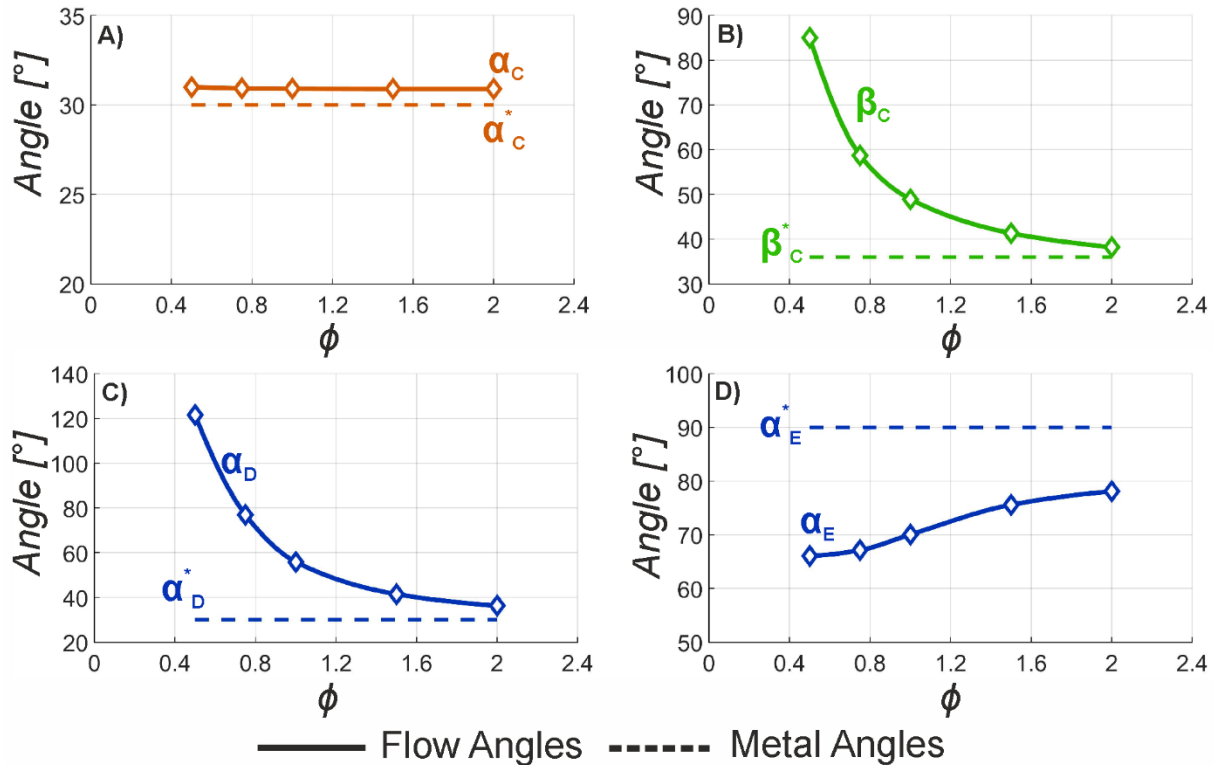
Figure 30 Outflow flow angles VS geometry angles in sections C, D, and E.

As shown in Figure 28, which corresponds to outflow mode, despite the reduction achieved in the optimized turbine, the OGV remains to be the second important source of losses. As been illustrated in Figure 31, the contours at the exit of the rotor are represented for both $\phi = 0.5$ and $\phi = 2$. Firstly, it should be mention that despite the large incidence at the inlet of the rotor for the lower flow coefficient (Figure 31.A), as mentioned previously (Figure 29), it has been damped within the rotor channel. This agrees with [29], where it is stated that for outflow radial turbines, the effect of the incidence at the rotor inlet, decays in the first half of the blade. However, for $\phi = 2$, where apparently the incidence of the flow is much better at the inlet (Figure 30.C and Figure 31.B) there is a strong flow detachment, produced by the curvature of the rotor blade, which is creating a large wake and generating a strong interaction between the rotor wakes and the OGV.

1   At last, the angle at the exit of the OGV (section E) is shown in Figure 30.D. It can be noticed
2   that the velocity that exits the OGV is not completely radial which would be an explanation for
3   kinetic energy losses at the exit. Nevertheless, from Figure 29, it is clear that the modulus of the
4   velocity due to the flow rate remains more important than this tangential component since the
5   loss due to kinetic energy increases almost linearly with the flow coefficient.

6
7   **Figure 31 Total pressure contours at section D for $\phi = 0.5$ and $\phi = 2$**
8   **with a colour map scale of 1:5, respectively.**
9

3.3.2 Inflow
10

11   Parallel to the analysis carried out for the outflow mode, this section analyses the performance
12   during inflow mode. Opposed to the outflow, the inflow starts from section F at the diffuser till
13   reaches section A, see Figure 5. The same sections as in the outflow are important for analysis,
14   section C and D are, respectively, the outlet and the inlet during inflow mode.

15
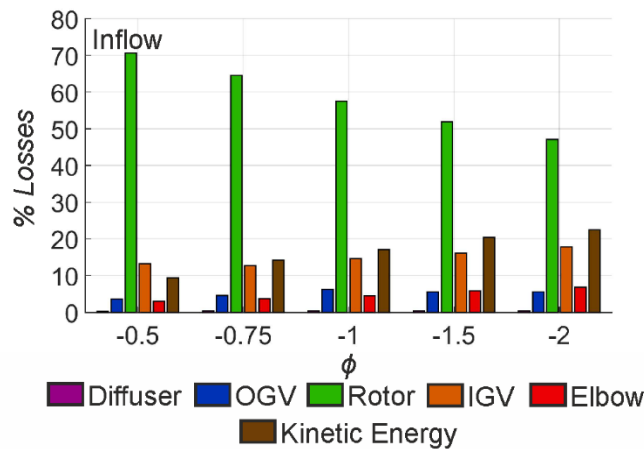
Figure 32 energy loss % in inflow process per turbine component.

Figure 32 shows the loss distribution per element whereas Table 5. shows the energy loss percentages for each element concerning the whole turbine, comparing the optimized turbine with respect to previous works [18].

The behaviour of energy losses of the rotor and the IGV are inversely proportional, the rotor has the major proportion of losses in all the flow coefficients but decreasing from 70% to 47% as the flow coefficient increases. Table 5. points out a large rise in the weight of the rotor loss, which is actually expected. Nevertheless, note that this large rise in the percentage is caused by an increase in the rotor loss, but also by the reduction of the overall loss of the optimized turbine.

The loss in the IGV is the real key to the improvement during inflow mode. There is a minimum in $\phi = -0.75$, from that, it can be seen as an increment in the losses as the flow coefficient raises, reaching almost 20% for the higher flow coefficient. Also, it is been noticed that despite the divergent geometry of the elbow before the outlet, the kinetic energy in this mode remains to be important at large flow coefficients.

Diffuser and OGV showed, as expected, an almost negligible weight of the energy losses with respect to the previous geometry as a result of the enhanced geometry of the OGV as mentioned before. The rotor revealed an increased percentage of losses concerning the whole turbine (previously illustrated in Figure 28), which is mainly due to the incidence angle at the inlet of the rotor. This phenomenon will be discussed later.

Linear increasing losses had been marked for the IGV along with the elbow section in both geometries (previous and optimized) but the relative loss percentage had decreased significantly in the optimized prototype, see Table 5.. This reduction is remarkably in the IGV section, reaching 20% approximately. Note that the loss percentages calculated in Table 5. are computed with respect to the input coefficient of each geometry (Figure 24). Also, clearly noticed that the high kinetic losses in the optimized prototype which is nearly the same as the previous geometry, thus the absolute loss has been reduced which proves that the divergent elbow has a positive effect, as expected.

1

Table 5. Previous geometry [18] **and optimized prototype energy losses percentage in inflow mode per turbine element**

	Previous geometry		Optimized prototype	
	$\phi = -0.5$	$\phi = -2$	$\phi = -0.5$	$\phi = -2$
Diff	0.04	0.05	0.20	0.30
OGV	4.18	6.95	3.60	5.60
Rotor	41.38	28.95	70.60	47.10
IGV	34.14	25.45	13.20	17.80
Elbow	10.00	16.22	3.00	6.80
Kinetic	10.26	22.38	9.40	22.40

Two total pressure contours around the gap between the OGV and the rotor, are shown in Figure 33, corresponding to low and large flow coefficients. It can be noticed in $\phi = -0.5$ (Figure 33.A) that the rotor channel is partially choked due to the flow detachment at the leading edge, resulting in a large magnitude for losses shown to be the strong gradient. Also at $\phi = -2$ (Figure 33.B) strong interaction between wakes and blade as a result of the larger area of section D with respect to the area of section C (Figure 5), accompanied by a thinner detachment at the leading edge unlike at $\phi = -0.5$, to explain these facts, insight of Figure 34 is needed, where the flow angles (relative and absolute) for section D have been plotted, in (A) can be noticed that the OGV guides the flow with an error of 2° only at the lower flow coefficient which is almost negligible. In (B), where the relative angle is shown and in accordance with Figure 33, the angle of the flow only is near the metal ones of the rotor at the higher flow coefficient, the point in which the detachment is thinner. For the rest of the flow coefficients, the difference between the angles is greater, driving a more powerful detachment on the suction side of the rotor blade.

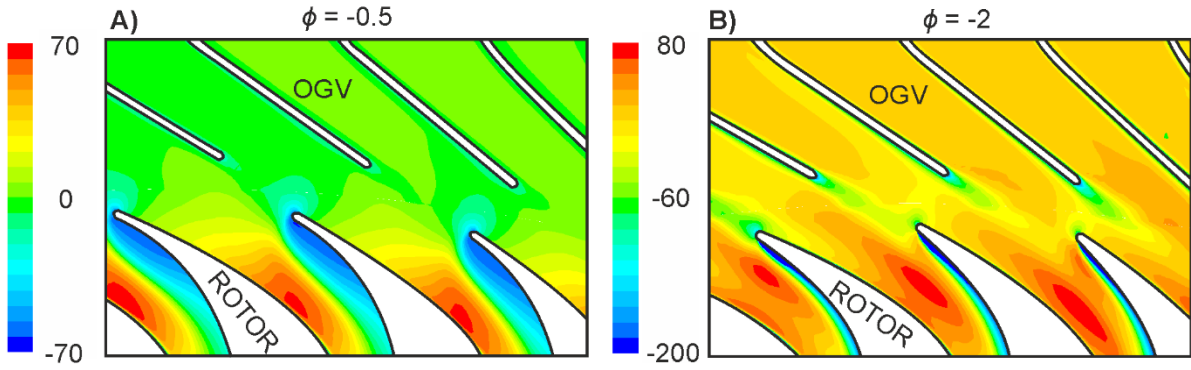**Figure 33 Total pressure contour at section D for $\phi = -0.5$ and $\phi = -2$ with a colour map scale of 1:2, respectively.**
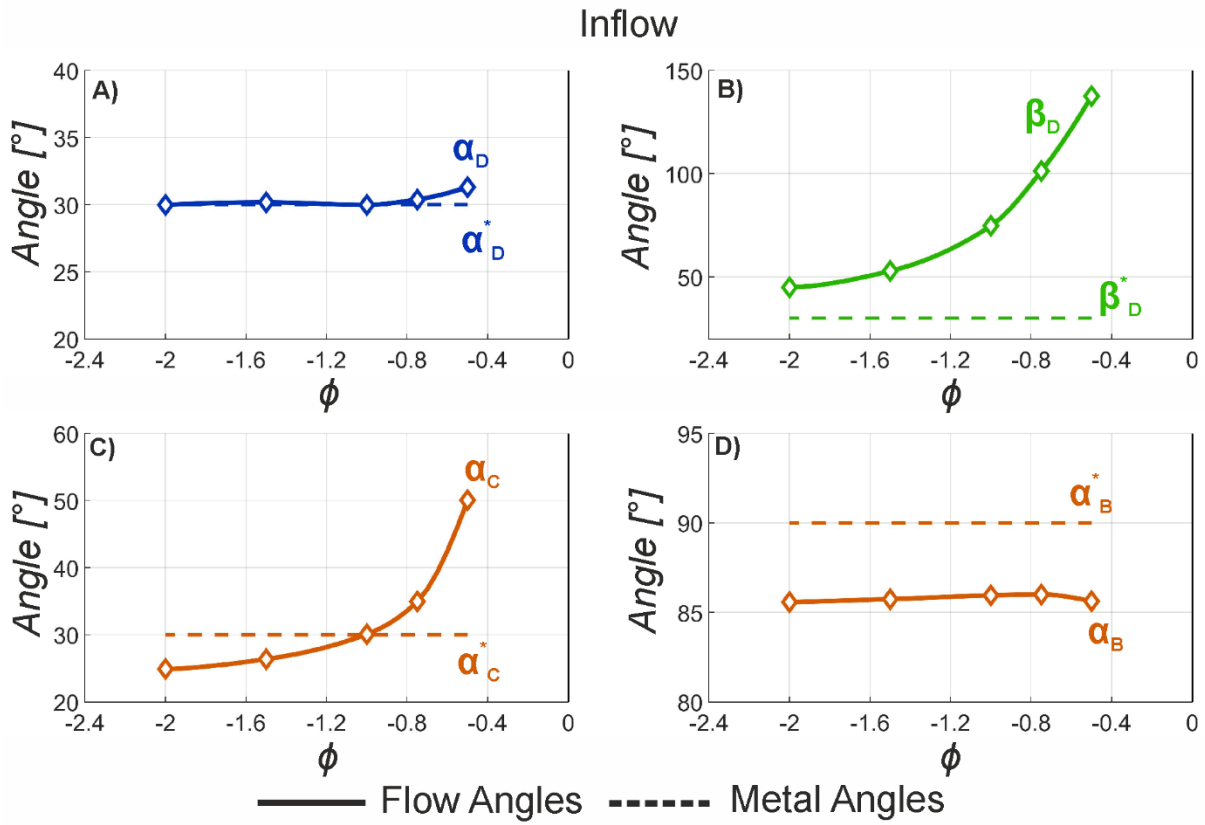

Figure 34 Inflow flow angles VS geometry angles in sections C, D, and B.

1   In Figure 35, the total pressure contours of the gap between the IGV and the rotor are plotted.

2   Can be noticed that for the lower flow coefficient (Figure 35.A) the detachment of the flow is

3   located in the pressure side of the IGV, but for the higher flow (Figure 35.B), the detachment

4   happens on the opposite face (suction side of the blade. Insight of Figure 34.C, the mismatch

5   changes the direction for points above $\phi = -1$ and below this point. In Figure 35.B detachment

6   wake changed sides from the pressure to the suction side assuring the phenomena in Figure 34.C.

7   It can be noticed that the reduction of the area of the section from D to C caused stronger

8   gradients at their limits, although helping the boundary layer to avoid detachment inside the rotor

9   passage. At last, in Figure 34.D the angle at the exit of the IGV is shown. To optimize the turbine

10   performance, the optimal angle at the exit should be as closer to 90° as possible. In this case, the

11   difference is below 5° in all ranges, which is almost negligible. Compared to the exit angle in the

12   outflow mode (α_E, see Figure 30.D), the IGV row guides the flow better having a lower

13   mismatch compared to the OGV row at the outflow mode.
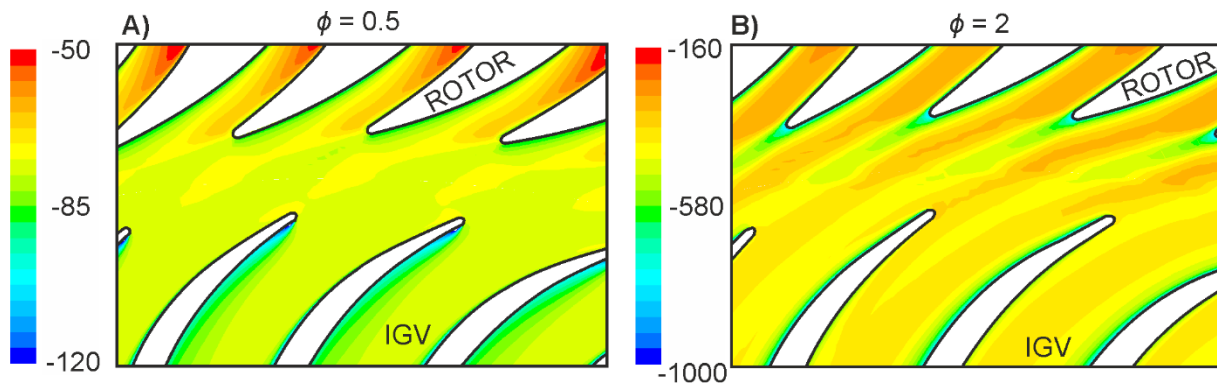
Figure 35 Total pressure contour in section C for $\phi = -0.5$ and $\phi = -2$

with a colour map scale of 1:12, respectively.

4. Conclusion

This work deals with radial impulse turbines for OWC systems, trying to optimize the design to close the gap with respect to axial impulse turbines. Based on previous CFD models, a new one with new features have been created to carry out the task of creating a new rotor design. The new CFD model, endorsed by software special tools for turbomachines, allows to speed up the simulation process and increase the reliability of the results.

This CFD model has been used to analyse a new turbine geometry, which is based on a different point of view. Since the radial impulse turbines available in the bibliography show that the loss downstream the rotor is the most critical point, the new rotor blade and setting angles of the guide vanes were set aiming to reduce the loss in the guide vanes, not in increasing the rotor efficiency. Besides, an analysis of the optimum solidity of each row, the rotor, and both rows of guide vanes. The solidities of the rotor and inner row of guide vanes have revealed themselves as critical, whereas the solidity of the outer row of guide vanes slightly affects the turbine performance.

The analysis of the results shows that the new configuration, as expected, present a lower rotor efficiency than previous geometries. The generation of incidence loss, larger than previous geometries, is the main cause of this decrease. On the other hand, both rows of guide vans have diminished notably the loss generated, especially when working downstream by the reduction of the incidence at the leading edge. Besides, since the deflection made by the guide vanes is lower, it allows to reduce the cord of the vanes and make wider the inter-vane passage, which reduces the loss generation when working upstream as well.

Concerning the global performance, the new geometry has higher efficiency during inflow conditions, without harming the efficiency during outflow efficiency. Nevertheless, the outflow performance remains to be the main drawback. The maximum steady efficiency during inflow performance has increased 11% with respect to previous geometries, whereas the improvement in outflow performance has reached a 2%. Speaking of non-steady efficiencies is where the real improvement managed by this new geometry is clearly seen. The new geometry has exceeded

the best of the previous geometries by almost a 7% in terms of maximum non-steady efficiency, whereas this difference is even overcoming for larger amplitudes of non-steady flow.

In summary, the new proposed geometry is a complete success when compared with respect to other radial impulse turbines for OWC systems. The efficiency has improved remarkably, and the damping has been reduced as well. Nevertheless, further study is needed to get closer to the best axial impulse turbine. The efficiency reached by axial turbines continues to be higher, but the results shown in this work are encouraging because the difference has been greatly reduced.

5. References

[1] I. Renewable Energy Agency, *INNOVATION OUTLOOK OCEAN ENERGY TECHNOLOGIES A contribution to the Small Island Developing States Lighthouses Initiative 2.0 About IRENA*. 2020.

[2] A. Clément *et al.*, "Wave energy in Europe: Current status and perspectives," *Renew. Sustain. Energy Rev.*, vol. 6, no. 5, pp. 405–431, 2002.

[3] J. Cruz, "Ocean wave energy: current status and future perspectives," *Choice Rev. Online*, vol. 45, no. 12, pp. 45-6810-45–6810, 2008.

[4] V. Jayashankar *et al.*, "A twin unidirectional impulse turbine topology for OWC based wave energy plants," *Renew. Energy*, vol. 34, no. 3, pp. 692–698, 2009.

[5] K. Mala *et al.*, "A twin unidirectional impulse turbine topology for OWC based wave energy plants e Experimental validation and scaling," *Renew. Energy*, vol. 36, no. 1, pp. 307–314, 2011.

[6] T. Setoguchi and M. Takao, "Current status of self rectifying air turbines for wave energy conversion," *Energy Convers. Manag.*, vol. 47, pp. 2382–2396, 2006.

[7] N. Ansarifard, A. Fleming, A. Henderson, S. S. Kianejad, S. Chai, and J. Orphin, "Comparison of inflow and outflow radial air turbines in vented and bidirectional OWC wave energy converters," *Energy*, vol. 182, pp. 159–176, 2019.

[8]   K. Kaneko, T. Setoguchi, and S. Raghunathan, "Self-rectifying turbines for wave energy conversion," *Int. J. Offshore Polar Eng.*, vol. 2, no. 3, pp. 238–240, 1992.

[9]   M. Takao and T. Setoguchi, "Air turbines for wave energy conversion," *Int. J. Rotating Mach.*, vol. 2012, 2012.

[10] T. Setoguchi, S. Santhakumar, M. Takao, T. H. Kim, and K. Kaneko, "A modified Wells turbine for wave energy conversion," *Renew. Energy*, vol. 28, no. 1, pp. 79–91, 2003.

[11] A. A. Wells, "Fluid driven rotary transducer," *Br. Pat. spec*, vol. 1, pp. 595–700, 1976.

[12] A. F. O. Falcão, J. C. C. Henriques, and L. M. C. Gato, "Air turbine optimization for a bottom-standing oscillating-water-column wave energy converter List of symbols," *J. Ocean Eng. Mar. Energy*, vol. 2, no. 4, pp. 459–472, 2016.

[13] R. P. F. Gomes, J. C. Henriques, L. M. C. Gato, R. P. F. Gomes, and J. C. C. Henriques, "Aerodynamic optimization of impulse turbine rotor blade cascades for wave power conversion," *Int. Conf. Ocean Eng.*, no. 2, pp. 15–17, 2008.

[14] T. K. Das, P. Halder, and A. Samad, "Optimal design of air turbines for oscillating water column wave energy systems: A review," *Int. J. Ocean Clim. Syst.*, vol. 8, no. 1, pp. 37–49, Apr. 2017.

[15] K. Elatife and A. El Marjani, "Optimization design procedure of a radial impulse turbine in OWC system," *Int. Energy J.*, vol. 18, no. 4, pp. 365–378, 2018.

[16] E. Otaola, A. J. Garrido, J. Lekube, and I. Garrido, "A Comparative Analysis of Self-Rectifying Turbines for the Mutriku Oscillating Water Column Energy Plant," *Complexity*, vol. 2019, p. 6396904, 2019.

[17] T. Setoguchi, S. Santhakumar, H. Maeda, M. Takao, and K. Kaneko, "A review of impulse turbines for wave energy conversion," *Renew. Energy*, vol. 23, no. 2, pp. 261–292, 2001.

[18] B. Pereiras et al., "An improved radial impulse turbine for OWC," *Renew. Energy*, vol. 36, no. 5, pp. 1477–1484, 2011.

[19] B. Pereiras, F. Castro, A. el Marjani, and M. A. Rodríguez, "Tip clearance effect on the

flow pattern of a radial impulse turbine for wave energy conversion," *J. Turbomach.*, vol. 133, no. 4, p. 41019, 2011.

[20] N. Ansarifard, S. S. Kianejad, A. Fleming, and S. Chai, "A radial inflow air turbine design for a vented oscillating water column," *Energy*, vol. 166, pp. 380–391, 2019.

[21] A. Thakker and T. S. Dhanasekaran, "Computed effects of tip clearance on performance of impulse turbine for wave energy conversion," *Renew. Energy*, vol. 29, no. 4, pp. 529–547, 2004.

[22] L. Rodríguez, B. Pereiras, M. García-Diaz, J. Fernández-Oro, and F. Castro, "Flow pattern analysis of an outflow radial turbine for twin-turbines-OWC wave energy converters," *Energy*, vol. 211, 2020.

[23] M. E. McCormick, J. G. Rehak, and B. D. Williams, "An experimental study of a bidirectional radial turbine for pneumatic wave energy conversion," in *OCEANS'92. Mastering the Oceans Through Technology. Proceedings.*, 1992, vol. 2, pp. 866–870.

[24] T. Setoguchi, S. Santhakumar, M. Takao, T. H. Kim, and K. Kaneko, "A performance study of a radial turbine for wave energy conversion," *Proc. Inst. Mech. Eng. Part A J. Power Energy*, vol. 216, no. 1, pp. 15–22, 2002.

[25] M. Takao, Y. Fujioka, H. Homma, T.-W. Kim, and T. Setoguchi, "Experimental study of a radial turbine using pitch-controlled guide vanes for wave power conversion," *Int. J. Rotating Mach.*, vol. 2006, 2006.

[26] L. M. C. Gato, A. R. Maduro, A. A. D. Carrelhas, J. C. C. Henriques, and D. N. Ferreira, "Performance improvement of the biradial self-rectifying impulse air-turbine for wave energy conversion by multi-row guide vanes: Design and experimental results," *Energy*, p. 119110, 2020.

[27] S. L. Dixon and C. A. Hall, "Fluid mechanics and thermodynamics of turbomachinery, 7th edition," *Fluid Mech. Thermodyn. Turbomachinery, 7th Ed.*, pp. 1–537, 2013.

[28] B. Pereiras, M. Takao, F. Garcia, and F. Castro, "Influence of the guide vanes solidity on the performance of a radial impulse turbine with pitch-controlled guide vanes," in

Proceedings of the International Conference on Offshore Mechanics and Arctic Engineering - OMAE, 2011, vol. 5, pp. 829–836.

[29] G. Persico, M. Pini, V. Dossena, and P. Gaetani, "Aerodynamic design and analysis of centrifugal turbine cascades," in *Proceedings of the ASME Turbo Expo*, 2013, vol. 6 C.

[30] S. W. T. Spence and D. W. Artt, "An experimental assessment of incidence losses in a radial inflow turbine rotor," *Proc. Inst. Mech. Eng. Part A J. Power Energy*, vol. 212, no. 1, pp. 43–53, 1998.

[31] N. Ansarifard, A. Fleming, A. Henderson, S. S. Kianejad, and S. Chai, "Design optimisation of a unidirectional centrifugal radial-air-turbine for application in OWC wave energy converters," *Energies*, vol. 12, no. 14, 2019.

[32] J. D. Denton, "Loss mechanisms in turbomachines," *J. Turbomach.*, vol. 115, no. 4, pp. 621–656, 1993.